Moiré control of multilayered graphene systems

Esmeralda Arreguin-Martinez

A thesis
submitted in partial fulfillment of the
requirements for the degree of

Master of Science

University of Washington
2023

Committee:
Matthew Yankowitz
Di Xiao

Program Authorized to Offer Degree:
Materials Science and Engineering

University of Washington

Abstract

Moiré control of multilayered graphene systems

Esmeralda Arreguin-Martinez

Chair of the Supervisory Committee:
Matthew Yankowitz
Department of Physics

Introducing a small rotation, or twist, between graphene multilayers gives rise to moiré patterns. At a certain magic angle, flat electronic bands are formed and the resulting structure gives rise to highly tunable correlated and topological states. To date, twisted graphene heterostructures comprising monolayer and/or bilayer graphene constituents have been shown to host isolated moiré flat bands. Moiré structures with more layers have not garnered much attention owing to the presence of additional bands that must be hybridized at low energy. This thesis will probe two graphene multilayer families: mixed dimensional moiré materials and double-twisted graphene multilayers. We find that the moiré can appreciably control the transport behavior of twisted graphene-graphite thin films and of an alternating twisted monolayer-trilayer-monolayer (t1+3+1) device. An inquiry of multilayered systems with higher band complexity is necessary in the search for superconductivity and novel correlated phenomena.

Table of Contents

List of Figures

Acknowledgements

First and foremost, I would like to express my gratitude to my committee members: Prof. Di Xiao for their time and valuable suggestions and to my advisor Prof. Matthew Yankowitz. I am particularly grateful to Matt for his guidance and encouragement over the course of my graduate studies. I came to the lab with zero experience in condensed matter physics. I feel incredibly lucky that you gave me the opportunity to work in your lab and for making sure I had the proper resources to be successful.

I also had the privilege of working with many talented individuals. I would like to give a special thanks to Ellis and Dacen. We worked very closely on many different projects, including the ones discussed here. You two were always willing to teach me new techniques in the lab and were always patient, offered guidance, and answered many of my questions in moments of confusion. Thank you to Chun-Chih, Anna, Manish, and Xuetao. I can't count the number of times you all have helped me take devices to the clean room. I'm grateful to have been part of a lab with such a strong collegial culture and disposition to help each other.

I would also like to thank the wonderful people who helped facilitate my move to the Materials Science department: Erin Kirschner, Robyn Davis, and Karen Wetterhahn. Without them I would not be here today and I am incredibly grateful for their patience and diligence in making sure everything was in perfect order. And a thanks to my mentors Prof. Maggie Werner-Washburne and Dr. Thomas Carmany who have remained invested in my future despite the constant career changes I have made throughout the years.

Lastly, my family. I would not be here without my parents. They have made many sacrifices in coming to this country for our sake. They managed to put not one, but three kids through college and I am incredibly grateful for their support throughout the years. I would also like to thank Carlos, Ruby, and Anthony, who have been constantly supporting me during

my Masters, and even packing me lunch on days when I was too busy. Lastly, I would like to give some love to my floofs, Duke and Chi who have lifted my spirits throughout the years. Los quiero mucho a todos.

Dedication

In memory of my grandparents, Mamá Pila y Papá Jesus

Chapter 1: Introduction

The most prominent material discovery of the century is graphene: a two-dimensional material composed of a single layer of carbon atoms[1]. It is the basic building block of graphite, carbon nanotubes, and buckyballs[1]. Although it was discovered in the 1970s, it was presumed not to exist in its isolated form until Andre Geim and Konstantin Novoselov at the University of Manchester were able to attain a single graphene film using adhesive tape[1,2]. For their discovery, they were awarded the Nobel Prize in 2010. The past two decades have expounded the remarkable physical and chemical properties of graphene. Among them are its high electrical and thermal conductivity, mechanical strength, and transparency[3]. The unique properties of graphene make it a material of great promise for applications in electronics, energy storage, and more[3].

So far, the field has seen rapid progress and has grown to include a number of other two-dimensional materials including black phosphorus, transition metal dichalcogenides (TMDCs), and hexagonal boron nitride (hBN)[4–7]. The renewed interest in two dimensional materials has opened avenues that were previously inaccessible. For example, new materials have been engineered by stacking monolayers of different 2D materials together where the properties of each layer can be leveraged to tailor materials with new and unique physical attributes[4,8–10]. Additionally, 2D materials that have been arranged in a twisted configuration with respect to another 2D material have revealed themselves to be ripe with novel physics[11–15]. With so many tuning parameters, the breadth of the field is large, and although many different structures have been studied to date, many materials in the two-dimensional design space remain unexplored.

The twisted graphene materials that have been studied in experiment so far are constructed from monolayer or bilayer graphene building blocks. The band structures of each are comprised of one set of linear and one set of parabolic bands respectively[16,17]. In such constructions, the pair of bands in momentum space deform at the magic angle and have a weak dispersion causing them to flatten. When we introduce more than two layers, we start introducing additional low energy bands residing at the Fermi energy and there is a question of whether they will hybridize at the magic angle. Theoretical studies have also shown that these additional bands can remain dispersive in nature, or in a special case, may even be able to hybridize[18–20]. However, it remains unclear how the electrical properties will be modified in the presence of additional bands. In this work we will investigate the behavior of graphitic materials with complex band structures. The two device configurations we will investigate are 1) graphene-graphite mixed dimensional systems where moiré interfaces are localized at the inner and outer surfaces and 2) double-twisted structures, namely t1+3+1, where an ABA trilayer is sandwiched between two graphene monolayers that are twisted to an equivalent angle relative to the ABA trilayer.

We will study twisted multilayered graphene with electrical transport measurements. Although we will only be taking measurements of resistance in our experiments, the measurements provide insights on the intricate relationships between the behavior of electrons and holes in a material. The quantum Hall effect (QHE) is a prime example where we can observe quantum mechanical phenomena at the macroscopic scale when we apply a magnetic field to a two-dimensional electron gas (2DEG). In QHE, the electrons begin to move in a highly ordered way and we see the resistance drop to a perfect value of h/e^2 (h-Planck's constant,e-elementary electric charge). As we will see, transport measurements are a useful tool to reveal quantum behavior.

The electronic properties of graphene

Electronic structure

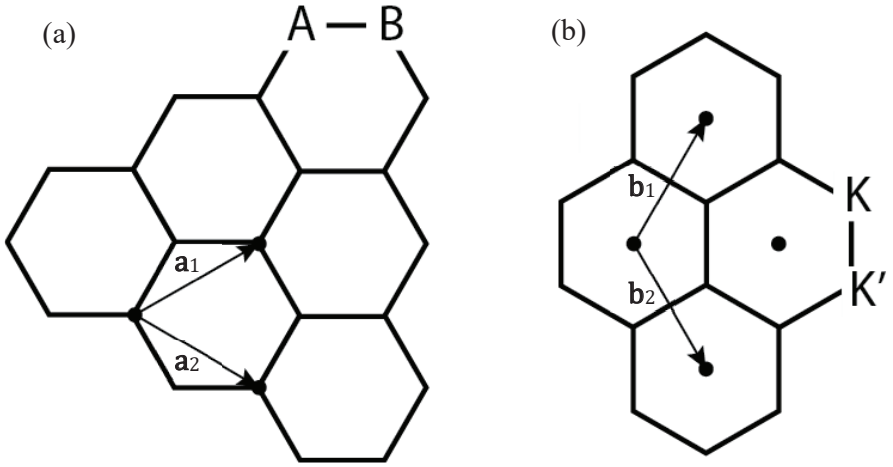

Figure 1. The graphene lattice structure. (a) The honeycomb lattice structure of graphene with a two-atom basis and its primitive lattice vectors $\mathbf{a}_1$ and $\mathbf{a}_2$. (b) The Brillouin zone depicting the K and K' points and primitive lattice vectors $\mathbf{b}_1$ and $\mathbf{b}_2$ of the reciprocal space.

We will first describe the structure of carbon. Carbon contains six electrons with a ground state configuration of $1s^2 2s^2 2p^2$. The two electrons in the $1s^2$ orbital are the core electrons and are electrically inert. The four electrons in the $2s^2$ and $2p^2$ orbitals, however, are available for bonding with other atoms. Thus, carbon has a tendency to form four bonds with neighboring atoms. In diamond, each carbon is bonded covalently to four neighboring atoms in a sp^3 hybridization and so its coordination number is n = 4. This results in a three-dimensional arrangement in the form of a tetrahedral lattice. Meaning, all four sp^3 electrons in the crystal occupy the bonding orbitals while the antibonding orbitals remain vacant. This gives diamond its wide bandgap and insulating properties.

In contrast, graphene has a coordination number of n=3, so we expect a carbon atom in graphene will form σ bonds with the three neighboring carbon atoms in the hexagonal plane. This leaves one lone electron in the p_z orbital that protrudes perpendicular to the lattice. The unhybridized p-orbitals of each atom will overlap to form delocalized π bonds. Most of the low

energy physics of graphene can be described by the wavefunction of the p_z orbital alone, considering the σ bonds are higher in energy and thus far away from the Fermi level. Therefore, we can use a tight binding model to describe the electronic properties of graphene.

The graphene lattice is of a bipartite nature. The structure consists of two lattice sites that define the unit cell. These are denoted as A and B in Figure 1a. The Bravais lattice vectors that describe the position of the A and B atoms are:

$$\mathbf{a}_1 = \left(\frac{3a}{2}, \frac{\sqrt{3}a}{2}\right) \quad \mathbf{a}_2 = \left(\frac{3a}{2}, -\frac{\sqrt{3}a}{2}\right)$$

The A and B sites are inequivalent and reflect the mirror symmetry of the sublattices. Here a is the carbon-carbon distance $a \approx 1.42$ Å. The unit vectors in the reciprocal space are thus defined as,

$$\mathbf{b}_1 = \left(\frac{2\pi}{\sqrt{3}a}, \frac{2\pi}{a}\right) \quad \mathbf{b}_2 = \left(\frac{2\pi}{\sqrt{3}a}, -\frac{2\pi}{a}\right)$$

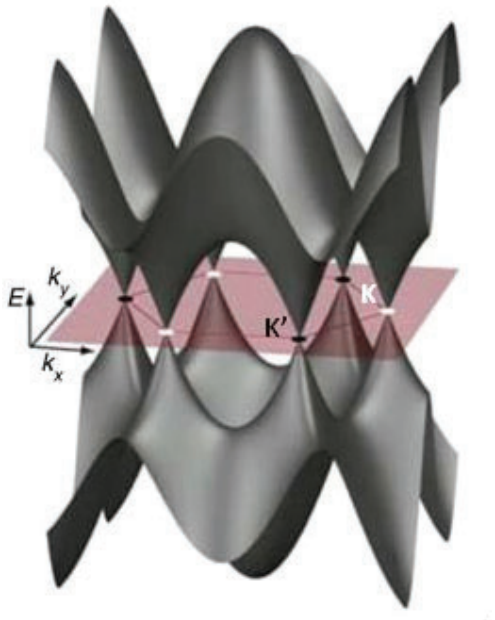

Figure 2. Energy spectrum of monolayer graphene depicting conic energy bands near the K and K' points. Adapted from[60].

shown in Figure 1b. The band structure can be calculated from the tight binding model as described in[16]. We can consider only the first nearest-neighbor terms for simplicity. The Hamiltonian can therefore be written as

$$H = -t \sum_{i,j} (a_i^\dagger b_j + \text{h. c.})$$

where i and j represent the nearest neighbor pair on different sublattices, and a_i (b_j) annihilates an electron while $a_i^\dagger$ ($b_j^\dagger$) creates an electron on sublattice A (sublattice B), and t is the hopping energy between nearest neighbors at approximately 2.8 eV. Ultimately, after solving for the eigenvalues of the Hamiltonian we find the energy bands are given by

$$E_\pm(k) = \pm t[3 + f(\boldsymbol{k})]^{1/2}$$

where

$$f(\mathbf{k}) = 2\cos\left(\sqrt{3}k_y a\right) + 4\cos\left(\frac{3}{2}k_x a\right)\cos\left(\frac{\sqrt{3}}{2}k_y a\right)$$

The energy bands meet at the K and K' points of the Brillouin zone (BZ) in Fig 1b, where $\boldsymbol{K} = \left(\frac{2\pi}{3a}, \frac{2\pi}{3\sqrt{3}a}\right)$ and $\boldsymbol{K'} = -\boldsymbol{K}$. Figure 2 illustrates the electronic dispersion of graphene and we can see linear crossings occur at the K and K' points. The linear dispersion is unlike other materials (which usually have a parabolic dispersion) and these bands resembles massless Dirac fermions as described by the Dirac equation[21]. We refer to these locations as Dirac points or valleys as they are the degenerate energy extrema of the valence and conduction bands. The ground state of monolayer graphene is thus four-fold degenerate from the valley pseudospin (2x) and from the electron spin (2x). Furthermore, in undoped graphene, the bands are exactly half-filled so the Fermi level is located precisely at the Dirac points where the valence and conduction bands

touch. Therefore, states at this charge neutrality point (CNP) only exist at the K and K' points. Since there is effectively no band gap, graphene is a semimetal.

Quantum Hall effect in graphene

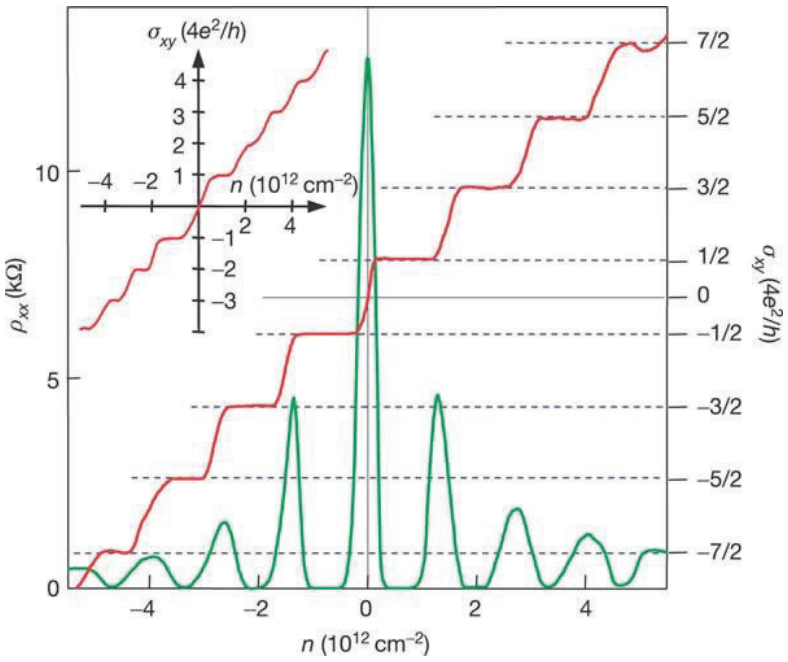

Figure 3. The Hall conductivity $\sigma_{xy} = R_{xy}^{-1}$ and resistivity ρ_{xx} of graphene as a function of carrier density. Inset shows σ_{xy} of Bernal bilayer graphene. Reprinted with permission[21].

The quantum Hall effect (QHE) is generally observed under extreme conditions in which strong magnetic fields are applied (causing broken time-reversal symmetry) and when the system is cooled down to near absolute zero temperatures. In experiment, the features that typically characterize the QHE are observed as a quantized transverse resistance R_{xy} and an associated drop in the longitudinal resistance $R_{xx} \rightarrow 0$ [22]. In the presence of a uniform perpendicular magnetic field B, charge carriers exhibit cyclotron motion in closed orbits. Quantization of the cyclotron orbits gives rise to Landau levels (LLs). In conventional materials where the wave function of electrons satisfies the Schrodinger equation, Landau levels are quantized into equidistant energy levels. However, we have seen that the dispersion of graphene is described by the Dirac equation. Therefore, the energy levels are not equally spaced since they are now

dependent on the density of states which varies linearly. The Landau level energies for monolayer graphene are given by the following,

$$\mathrm{E_N} = \pm \mathrm{v_F}\sqrt{2\mathrm{e}\hbar\mathrm{B}|\mathrm{N}|}, \mathrm{N} \in \mathbb{Z}$$

where $\mathrm{v_F}$ is the Fermi velocity and $\hbar$ is the reduced Planck's constant.

The QHE has an expected Hall conductivity of $R_{xy}^{-1} = 4N\frac{\mathrm{e}^2}{\mathrm{h}}$. The factor 4 reflects the LLs at K and K' and the two-fold spin degeneracy. However, in graphene, the plateaus are observed at half-integer filling where the first plateau is at $2\mathrm{e}^2/\mathrm{h}$, whereas in the conventional QHE it should be observed at $4\mathrm{e}^2/\mathrm{h}$ (Figure 3) [21]. This means the N = 0 Landau level will be shared equally by electrons and holes. The sequence will therefore be

$$R_{xy}^{-1} = 4\left(N + \frac{1}{2}\right)\frac{e^2}{h}$$

where the filling factor is

$$\nu = 4\left(N + \frac{1}{2}\right) = (\pm 2, \pm 6, \pm 10 \ldots).$$

Bernal bilayer graphene

Next, we can consider adding an additional monolayer on top of graphene. There are a couple of ways this can be done. Either we can have a bilayer where the atoms in the A and B sites sit directly on top of each other, referred to as AA stacking, or alternatively the atoms can be aligned so that the A sites reside directly on top of the B sites. The latter is referred to as AB stacking or Bernal stacking and is energetically more favorable and thus found more commonly in naturally occurring graphitic films.

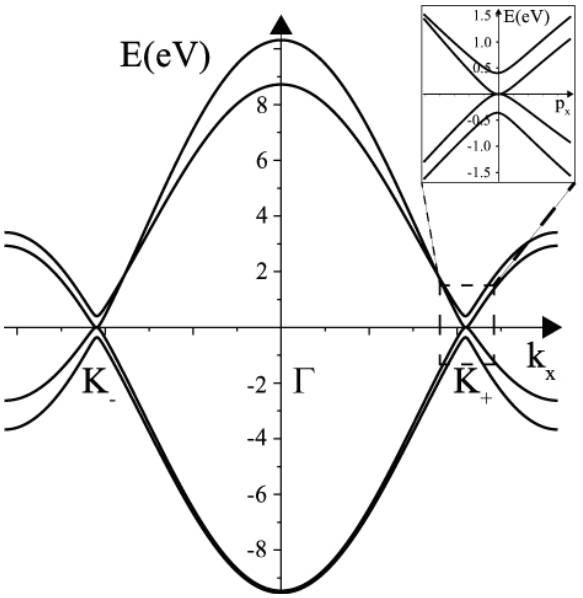

Figure 4. Electronic bands of bilayer graphene. Inset depicts close-up of the low-energy bands. Reprinted with permission[17].

Like monolayer graphene, the energy dispersion of Bernal stacked bilayer (BLG) can be described by the tight binding model. We will forgo a thorough analysis here, but refer the reader to the following reviews[17,23]. We again have annihilation and hopping terms, but in addition to in-plane hopping $\gamma_0 = t$, we also consider hopping energy between sites on the different layers. We consider hopping between the A site of the first layer (A1) and the A site of the second layer (A2), γ_1, the hopping energy between the B sites (B1 and B2), γ_3, and the hopping energy γ_4 between A1 and B2, and A2 and B1. The Hamiltonian is the following where m is the layer number and σ is the spin

$$H = -\gamma_0 \sum_{\langle i,j\rangle,m,\sigma} \left(a^{\dagger}_{m,i,\sigma} b_{m,j,\sigma} + \text{ h.c. }\right) - \gamma_1 \sum_{j,\sigma} \left(a^{\dagger}_{1,j,\sigma} a_{2,j,\sigma} + \text{ h.c. }\right)$$
$$-\gamma_3 \sum_{j,\sigma} \left(b^{\dagger}_{1,j,\sigma} b_{2,j,\sigma} + \text{ h.c. }\right) - \gamma_4 \sum_{j,\sigma} \left(a^{\dagger}_{1,j,\sigma} b_{2,j,\sigma} + a^{\dagger}_{2,j,\sigma} b_{1,j,\sigma} + \text{ h.c. }\right).$$

The tight binding Hamiltonian can be diagonalized to obtain the energy spectrum of bilayer graphene which is depicted in Figure 4. As opposed to graphene, the low energy dispersion in BLG is quadratic and the interlayer coupling leads to the presence of massive chiral quasiparticles[24].

As a result, the LL energy for bilayer graphene can be described as

$$\mathrm{E_N} = \pm\hbar\omega_c\sqrt{\mathrm{N(N-1)}}, N \in Z.$$

ω_c is the cyclotron frequency eB/m^* where m^* is the effective mass. The Landau sequence is linear in field, like monolayer, but we can appreciate the sequence arises from degenerate Dirac points at the CNP making the zero-energy level eightfold-degenerate[24–27].

The tunability of van of der Waals materials

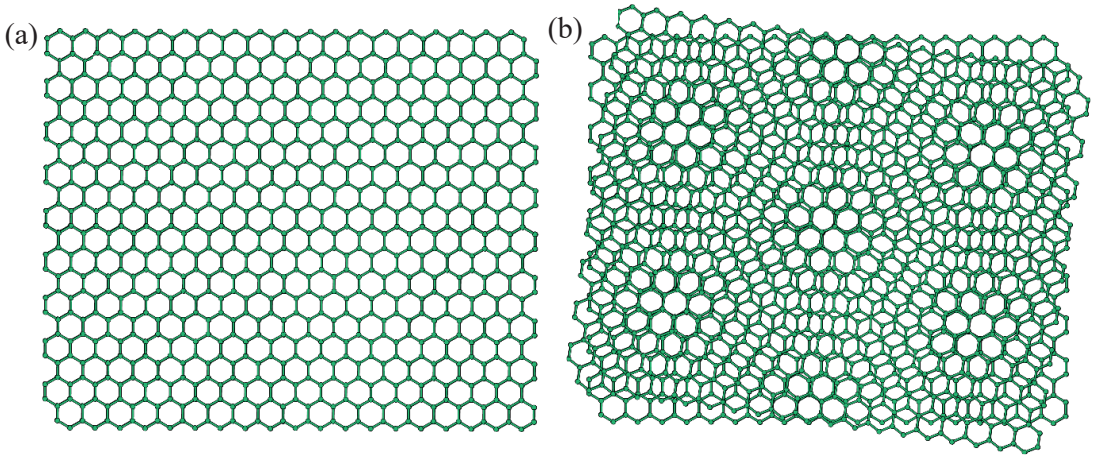

Figure 5. Graphene hexagonal lattice depicting (a) monolayer graphene and (b) twisted bilayer graphene with an emergent moiré pattern.

Van der Waals stacking

Two dimensional materials consist of vertically stacked layers that are held together by the weak van der Waals force. This property allows us to easily separate individual layers (discussed in Chapter 2) and engineer materials in an endless number of ways[4,28]. There are some advantages of being able to separate and assemble materials layer by layer. For example, efforts to bring about proximity-induced ferromagnetism or spin-orbit coupling have been investigated by combining 2D materials such as the atomically flat yttrium iron garnet or the chromium trihalides (CrI_3, $CrBr_3$, etc.) and monolayer graphene[29–31]. Another example is the more widely studied transition metal dichalcogenides MoS_2/WSe_2 and $MoSe_2/WSe_2$

heterostructures. These materials have different work functions and therefore combining the two can lead to the separation of electrons and holes into different layers[32–34]. Another commonly used van der Waals materials is boron nitride (BN). BN is extensively used as a dielectric insulator in graphene-based devices and has many favorable properties as will be described in the following sections.

Twist angle

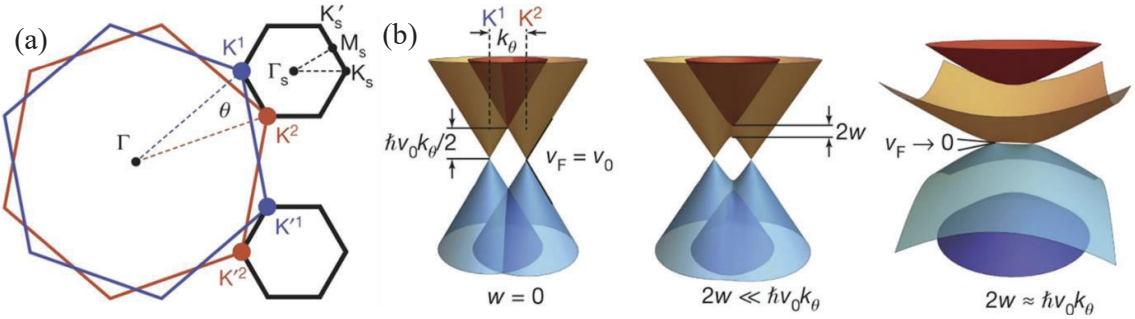

Figure 6. Band structure of twisted bilayer graphene. (a) The mini-Brillouin zone and (b) the hybridization of Dirac cones and materialization of the flat bands. Reprinted with permission[11].

By now we know that even the addition of one layer atop graphene can affect the overall electronic properties. We can go further and ask: What happens if we 'twist' one atomically thin sheet on top of the other? In real space a beautiful geometric pattern emerges that creates a long-range pattern, or moiré, which arises from the mismatch of the crystal lattice. In Figure 5b, the light areas correspond to regions that are locally AA stacked and the darker regions are AB or BA stacked. The moiré wavelength λ is associated with the length scale of these regions and is a function of the twist angle θ and the graphene lattice constant $a = 0.246$ nm. Near a 'magic' twist angle, the moiré wavelength can become much larger than the atomic lattice length scales and can drastically modulate the electronic structure of graphene.

We can understand the modulation by looking in momentum space. The mini-Brillouin zones of a twisted bilayer are depicted in Figure 6a. These folded mBZs are a direct result of

the moiré potential and are defined by the offset of the K or K' wavevectors of each layer. At the K points, the energy dispersion comprises two overlapping Dirac cones. One corresponds to the K point of the top layer, and the other corresponds to the K point of the bottom layer. We likewise see this overlap for the Dirac points at the K' locations. As we approach the magic angle of 1.1°, the interlayer coupling becomes stronger and the low energy bands deform, becoming extremely flat[35]. If we look at the band structure, the band is now isolated with gaps above and below the mBZ at the crossing points of the Dirac cones (Figure 6b). The condition where the bands become flat correspond to a vanishing Fermi velocity v_F. The Fermi velocity becomes zero and electron-electron interactions will dominate due to the competition between the Coulomb energy and the kinetic energy of the electrons. It is in this regime where we can see unconventional interaction-induced states.

Electric field effect

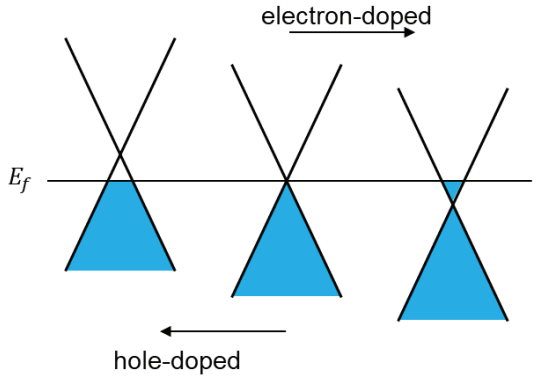

Figure 7. Schematic illustration of the manipulation of the Fermi level as we gate a graphitic system.

The capacitive field effect is an electrical property where an applied electric field generates a potential difference across a material. The field effect works through the manipulation of the Fermi level, which acts as a dividing line between the occupied and unoccupied electronic states of the material (Figure 7). Depending on the strength of the applied electric field, the Fermi level can shift between the conduction band and the valence band. When the Fermi level

is in the valence band, the density of the charge carriers decreases while a shift toward the conduction band will increase the density of the charge carriers.

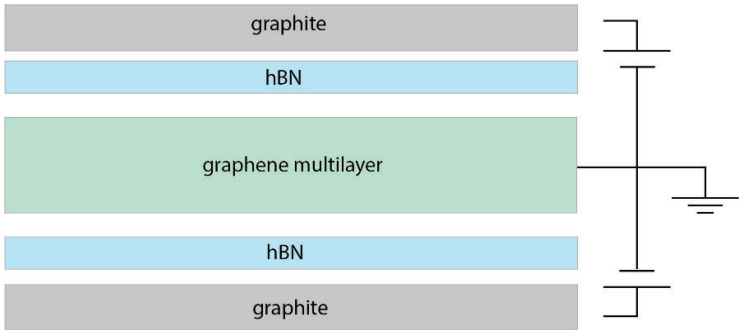

Figure 8. Graphene device geometry depicting the dielectric encapsulating layers (BN) and gate electrodes (graphite) that allow for carrier and displacement field tuning.

The charge carrier density and displacement field D of graphene can be independently tuned by applying an external gate voltage to devices that are typically encapsulated between two flakes of hexagonal boron nitride and two metal gates (Figure 8). Graphite electrodes are commonly used as gates to dope systems of graphitic materials as reduced sample disorder has been observed[36]. Similarly, the choice of using BN as a dielectric substrate is intentional and has become standard practice to produce high quality graphene-based devices[8]. Like graphene, BN is a two-dimensional material with a hexagonal crystal structure, except boron and nitrogen atoms occupy the A and B sublattice sites. But although similar, BN is an insulator with a large band gap of about 5.97 eV owing to the different on-site energies of its atoms[37]. Since the lattice of hBN is free of dangling bonds and has a high phonon energy, the charge disorder in graphene is minimized compared to graphene on silicon substrates, which were typically used in the early days of the field[38]. Overall, the choice of substrates minimize disorder artifacts and provide the necessary conditions to successfully tune graphitic devices.

Twisted graphene structures

The modified physics of moiré graphene systems manifests itself in the properties that characterize the materials. Over the course of a few years we have learned that twisted materials

are ideal platforms for attaining correlated insulators, anomalous Hall effect, and other topological states[11,39–42]. In the case of tBLG, several unconventional states have been found that are a directly driven by electron-electron interactions. Under the right conditions, tBLG can behave as a metal, insulator, or a superconductor. The superconducting (SC) state is a correlated phenomenon that is characterized by zero resistance, sharply switching V-I curves, and quantum coherence[12,13,43–45]. In tBLG at the magic angle of 1.1°, insulating states are notably found at half-filling of the moiré in both the conduction and valence bands. These gaps are not predicted by the single-particle band calculations and correlate strongly with a narrowing of the bandwidth of the low energy bands[11,12]. Furthermore, the superconducting regions emerge near the insulating states at integer fillings. These superconducting phases have proved to be tunable by adjusting the charge carrier density, magnetic field, and pressure[12,13,45].

The discovery of the tBLG electrical properties has led to a frenzy of research and many structures have been theoretically and experimentally explored. For example, magic angle twisted trilayer graphene (MATTG), tetra- (MAT4G), and penta-layer (MAT5G) graphene are a group of structures that have a back-and-forth alternating sequence of a rotation θ between successive layers. These structures have all also been shown to host correlated insulators and superconductivity[44–47]. There is some speculation that the shared symmetries of this alternating twist graphene family, including tBLG, can play a role in establishing a robust superconducting state, although its exact origin is still subject to debate.

The other twisted graphene structures that have been investigated so far are twisted double bilayer graphene (tDBG) and twisted monolayer-bilayer graphene (tMBL). Unlike the alternating twist devices, superconductivity has not been seen in tMBL and tDBG so far[14,48–51]. To summarize, the tDBG did not show SC states but exhibited correlated insulating states in the conduction band when a finite displacement field D was applied. Band calculations show

that as a D field is applied, the bandwidth of the conduction band becomes smaller while the valence band becomes more dispersive. The ability to tune this device with D, is a result of the broken C_2 symmetry and is applicable to any device with a twisted M+N structure where at least one component (M or N) is a Bernal bilayer or thicker multilayer.

The tMBG that has been studied recently also shares this tunability. The paper by Chen et. al.[14] shows that their tMBG structure breaks the two-fold symmetry rotation as well as the mirror reflection symmetry. Therefore, tMBG is sensitive to the sign of the perpendicular displacement field. When the field is in the direction pointing from the bilayer to the monolayer sheet ($D < 0$), the density of states is suppressed in the outermost sheet of the bilayer and correlated states are seen at every integer filling factor. When $D > 0$ and in the direction from the monolayer to the bilayer, the tMBG has an enhanced density of states on the outermost bilayer and we see a spin-polarized correlated state emerge at half-filling. Taken as a whole, these two tunable states in tMBG reflect features observed in twisted bilayer graphene or twisted double bilayer graphene and is dependent on the sign of the displacement field.

Chapter 2: Device Fabrication and Methods

Figure 9. Optical image of AFM-cut exfoliated graphene multilayers on an SiO_2 substrate. Light regions are monolayer graphene, while the dark area is a trilayer graphene.

Constructing a two-dimensional stack

Exfoliation

The 2D sheets that make up a bulk graphite crystal are held together by the weak van der Waals force, therefore simple mechanical means, such as mechanical exfoliation with scotch tape, can be used to separate the layers down to one or a few atoms thick. First, a graphite crystal is set on a clean area on the sticky side of the tape. The tape is then pressed on and pulled off from the crystal repeatedly to isolate graphene layers from the bulk crystal. The tapes are placed on a plasma-cleaned silicon wafer substrate with a 285 nm silicon dioxide layer. To increase the yield of the exfoliated graphene flakes, a baking step at 110 °C is performed before the tape is removed from the substrate. The flakes are inspected with an optical microscope to distinguish the thickness of the layers by looking at the phase contrast between the flakes and the SiO_2 substrate. When making multilayered devices, it is important to select a single flake which contains both monolayer and multilayer regions to guarantee they are in an identical crystal orientation. Next, flakes with monolayer and multilayer regions are cut with the tip of an atomic

force microscope (AFM) in preparation for the next steps. For example, the flake in Figure 9 contains regions that have one layer (lighter regions) and three layers (darker region). The outer areas along the edges are cut into "fingers" with the purpose of creating enough friction between the stacked sheets to increase the probability of achieving the target twist angle while avoiding relaxation during the transfer process.

Transfer technique

The process of transferring graphene flakes from one substrate to another has improved considerably over the years. An early method involved directly exfoliating flakes onto a substrate coated with a polymer[38]. A water-soluble layer resided in between the polymer and chip, where the polymer containing the graphene flake of interest could be isolated in a water bath, positioned on top of another flake to create heterostructures, and finally placed in a solvent to remove the polymer. The technique used in the present work, however, entails picking up layers with a homemade stamp and transferring them to a clean SiO_2 substrate[52]. Heterostructures using this dry-transfer process are cleaner since only the topmost flake is exposed to polymer. The general steps are illustrated in Figure 10. A transfer stage, with high precision actuators, is used in combination with a stamp to pick up and align flakes. The stamp is made of a polydimethyl siloxane (PDMS) dome with a thin layer of polymer, namely polycarbonate (PC), covering the surface. The stamp is used to press down (step 1) and pick

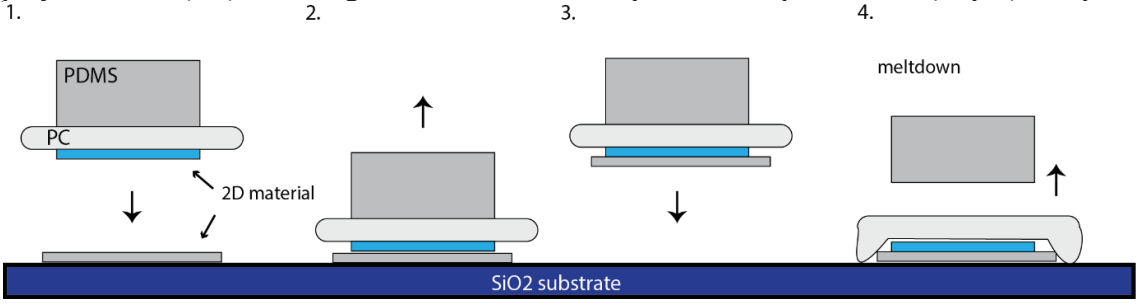

Figure 10. Illustration of the dry transfer steps used to assemble layers of 2D materials.

up hBN or graphene/graphite flakes (step 2 and 3). In addition, the stamp is heated during the pick-up and encourages the adhesion of graphene to the PC film. Subsequent flakes of graphene

multilayers or BN can be picked up on the same PC and then melted down on to the Si substrate (Figure 10, step 4). Lastly, the PC is dissolved in chloroform and the multilayer graphene stack remains on the silicon substrate (Figure 11a).

Nanofabrication

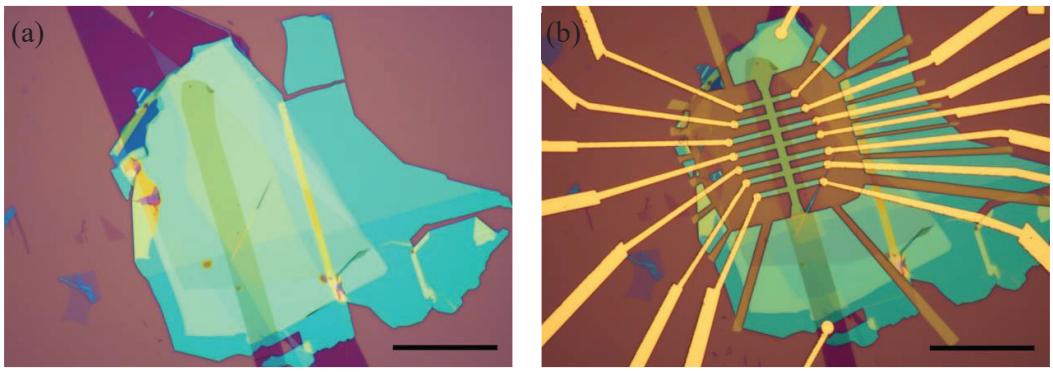

Figure 11. Optical images of (a) graphene-hBN stack and of (b) final device after completion of all nanofabrication steps. Scale bars: 25 μm.

Once a device stack is assembled, it undergoes a series of standard fabrication steps to create the contact geometry needed to construct a measurable device. Electron beam lithography is a technique used to pattern sub nanometer features on a substrate coated with a photoresist. Areas of the resist that are exposed to the electron beam increase in solubility and can be washed away with a developer. The remaining resist acts as a mask for the next steps in the process to etch the device into a suitable geometry and deposit a conducting metal to define the contact leads.

First, a double layer of the photoresist, poly(methyl methacrylate) (PMMA), is spin-coated on the silicon substrate. A495K PMMA is spin coated first, baked, and followed by A950K PMMA and another baking step. The A495K PMMA is more electron sensitive compared to A950K PMMA and is purposely spun first to create an undercut in the dual coated resist when it is exposed to the electron beam. The undercut facilitates the metal-liftoff process later down in the pipeline.

Next, a TESCAN scanning electron microscope with electron beam lithography (EBL) capability (with 30kV and an e-beam dose of 350 $\mu C/cm^2$) was used to define the Hall bar geometry of the device. BN and graphene layers are subsequently etched using CHF_3 and O_2 plasma etching. EBL is used again to define the contact leads followed by metal evaporation. For evaporation, a thin layer of chromium, on the order of 7nm, is deposited first as an adhesive layer before depositing 70-100nm of gold. The unwanted gold is removed during the lift-off process where an acetone bath dissolves the PMMA, revealing the final device configuration (Figure 11b).

Measurements and data interpretation

The body of the work described here will focus on measurements of resistance. As illustrated in Figure 8, our devices are assembled into dual-gated devices using the stacking technique. We have BN encapsulated twisted graphene/graphite enclosed by top and bottom graphite gates. First, I will describe how the devices are prepared and measured and later I will discuss the details of how we determine key quantities for our measurements.

To prepare the fabricated devices for measurement, the SiO_2 substrate holding the device is diced into a small square and fixed into a dual in-line package (DIP) socket with silver paste. The device is subsequently wire bonded to the chip carrier and devices undergo preliminary testing. This is done first at a room temperature probe station to assess whether contacts are functional and if the graphite gates are isolated from the graphene multilayers. In our experiments, the device is cooled down to cryogenic temperatures on the order of 1K. Transport measurements are performed in a four-terminal geometry where the voltage between two contacts is measured while an AC current excitation of 10 nA or 100 nA is applied with a lock-in amplifier at a frequency of 17.7 Hz. In twisted multilayer devices (t1+3+1 and t3+1+3), an Si gate voltage was applied so that a shift to a high charge carrier density and a reduction in contact resistance occurs.

In general, measurements of resistance R are taken to characterize the transport properties of the sample of interest where

$$R = \frac{Voltage\ (V)}{Current\ (I)}.$$

Devices are fabricated in a dual-gated configuration (Figure 8) to independently tune the displacement field (D) and charge carrier density (n). This is achieved by applying top and bottom gate voltages where

$$n = \frac{V_{\mathrm{tg}}C_{\mathrm{tg}} + V_{\mathrm{bg}}C_{\mathrm{bg}}}{e}$$

and

$$|D| = \left|\frac{V_{\mathrm{tg}}C_{\mathrm{tg}} - V_{\mathrm{bg}}C_{\mathrm{bg}}}{2}\right|$$

where C_{tg} and C_{bg} are the top and bottom gate capacitances and e is the electron charge.

Twist angles are determined by the formula,

$$n_{\mathrm{s}} = 8\theta^2/\sqrt{3}a^2$$

here n_{s}= ±4 = ν is the charge carrier density where insulating states are observed and a= 0.246 nm is the lattice constant of graphene. $\pm n_{\mathrm{s}}$ is obtained from the projection points of quantum oscillations in a magnetic field. Alternatively, Brown-Zak (BZ) oscillations that appear in the Landau fan diagram can also be used as a measure of the twist angle[53–55]. At magnetoconductance peaks, the magnetic flux $\varphi = 4B/n_{\mathrm{s}}$ is equal to $\frac{p}{q}\varphi_0$. Here, $\varphi_0 = h/e$ where h is Planck's constant, and p/q are integers. We can therefore obtain n_{s} by fitting the magnetoconductance peaks to a series of rational φ/φ_0.

Chapter 3: Electrical transport in mixed-dimensional systems

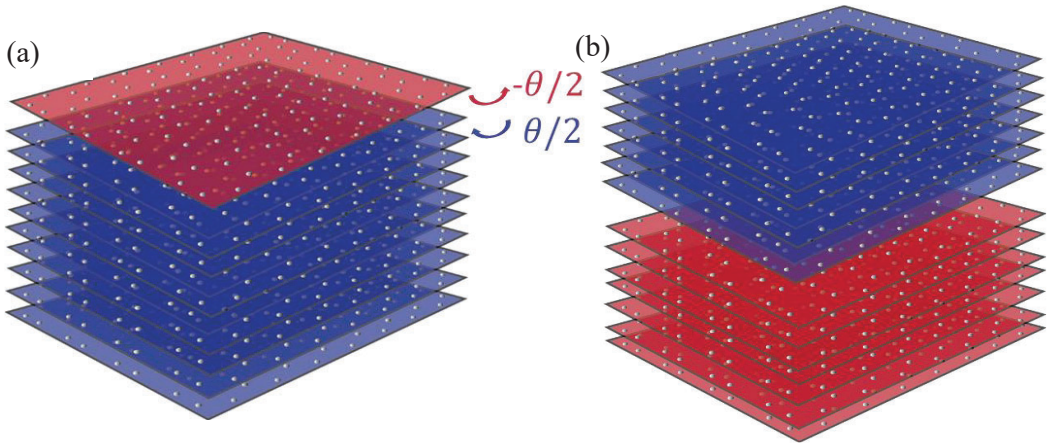

Figure 12. (a) Cartoon schematic of (t1+Z) monolayer graphene (red) twisted at an angle θ relative to a graphitic film (blue) and (b) two thin films (t7+7) of Bernal graphite twisted at an angle θ relative to each other.

So far, the study of moiré materials has remained with a strong focus in ultra-thin van der Waals systems as we have discussed previously. Those studied to date include the alternating twisted graphene family (with up to 5 graphene monolayers), twisted bilayer-bilayer and twisted monolayer-bilayer graphene[11,46,49,51]. Probing the realm of thicker structures has evaded research efforts likely due to the added complexity with more bands present at low energy as more layers of graphene are added. Yet, theoretical studies show flat bands are observed for small twist angles in systems where a stacking fault is situated within a stack of semi-infinite graphite crystals or when a single graphene layer is rotated atop a graphite stack[56]. However, there has remained a level of uncertainty as to whether there will be appreciable modification of transport properties until now.

We have shown that the incorporation of a moiré at the surface of a graphite thin film can modify the electronic properties of an entire graphene-graphite system[57]. Dual-gated devices of Bernal graphite and devices of a rotated sheet of graphene on Bernal graphite were

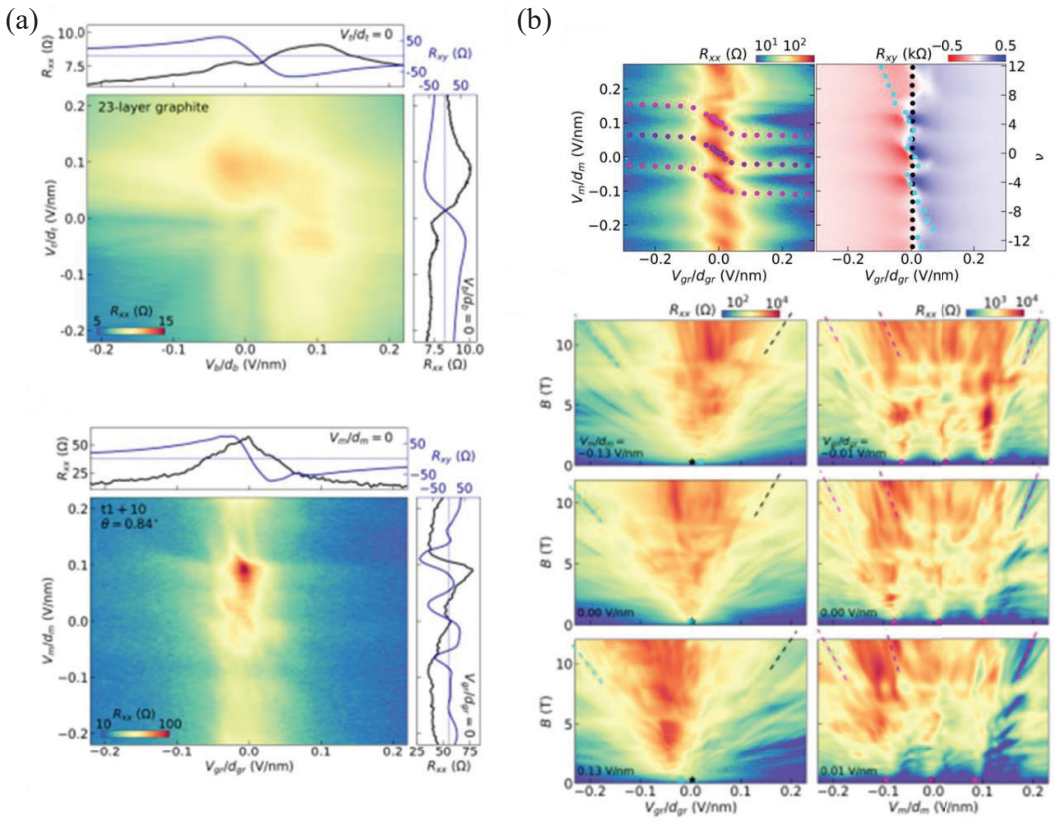

Figure 13. (a) Zero-field transport of 23-layer grahite (top) and t1+10 (bottom) devices. (b) Longitudinal (left) and Hall (right) resistance maps of t1+10 device acquired at B = 0.5 T. Zero-field projections of QOs from the V_{gr} Landau fans (bottom left panel) are overlayed onto the Hall resistance map. The projection points of the V_m Landau fans (bottom right panel) are plotted in the longitudinal resistance map. Adapted from[57].

made ranging between 6 and 40 layers thick (Figure 12a). If we consider the standalone thin film of Bernal graphite, consistent features were observed in the resistance maps as a function of top and bottom gate voltages. For instance, there is a single sign change in the Hall resistance (R_{xy}) when the back gate (V_b) is held constant and the top gate (V_t) is swept, and likewise there is only one sign change when V_t is held constant and V_b is swept (Figure 13a, top).

Transport in a 10-layer Bernal graphite device with a monolayer of graphene rotated at an angle of 0.84 deg (t1+10) shows a markedly different behavior in transport as each gate is tuned (Figure 13a, bottom). When tuning the gate closest to the graphite surface (V_{gr}), we see a single peak in the longitudinal resistance centered around $V_{gr} = 0$ and a single sign change in

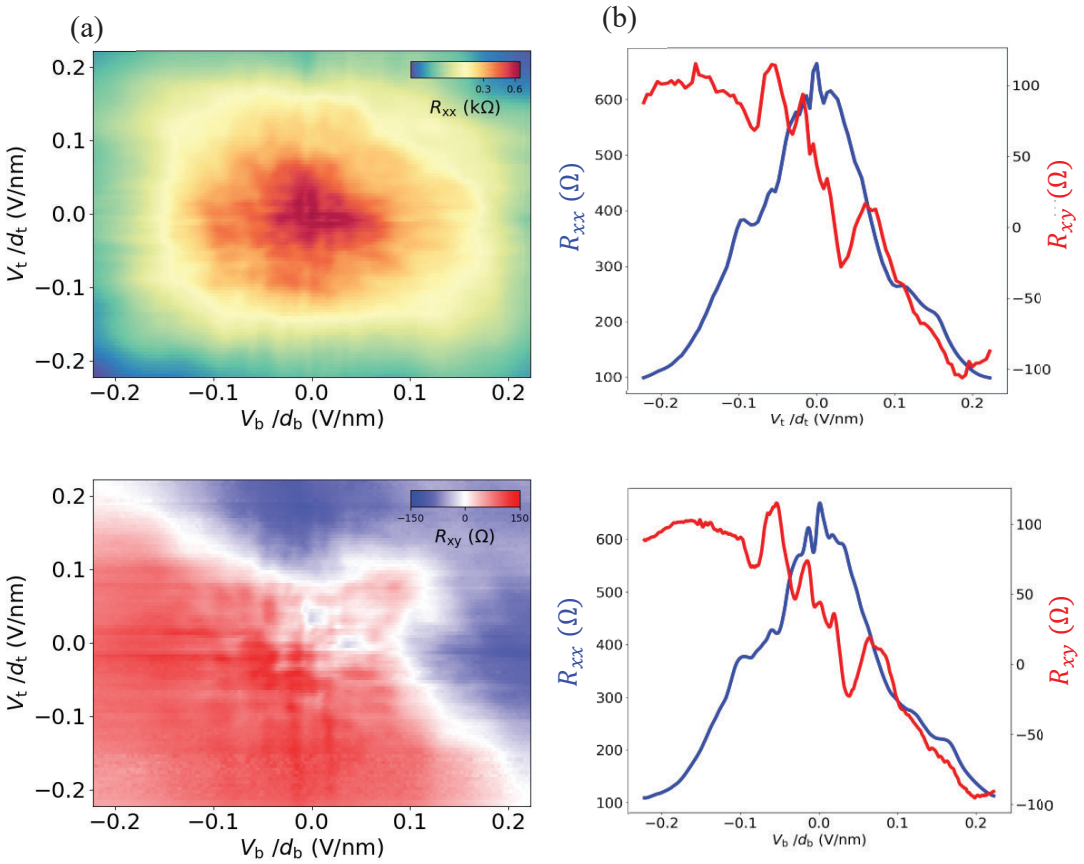

Figure 14. Low field magnetotransport of t7+7 device. (a) Longitudinal (top) and Hall (bottom) resistance as a function of top and bottom gate voltages. (b) Line cuts of R_{xx} and R_{xy} when $V_b = 0$ (top) and when $V_t = 0$ (bottom).

R_{xy}. This is similar to what we observe in Bernal graphite. However, when the gate closest to the moiré interface (V_m) is tuned, several sign changes in R_{xy} occur tracing out an unusual zig-zag pattern near $V_{gr} \approx 0$ indicating a switch in the charge of free carriers. Furthermore, peaks in resistance (R_{xx}) form at what we would consider the CNP and full filling of the moiré bands (Figure 13b, top left). Ultimately, the transport in these systems is mediated by a combination of surface states and intrinsic bulk states that can be describe by screening effects from bulk graphite[58]. Essentially, the surface moiré states are tunable when a gate voltage is applied while the graphite bulk remains as a compensated semimetal, meaning the electron and hole doping will remain roughly constant and therefore not respond to gating. This conclusion is further corroborated by a four-component Drude transport model that agrees with transport results

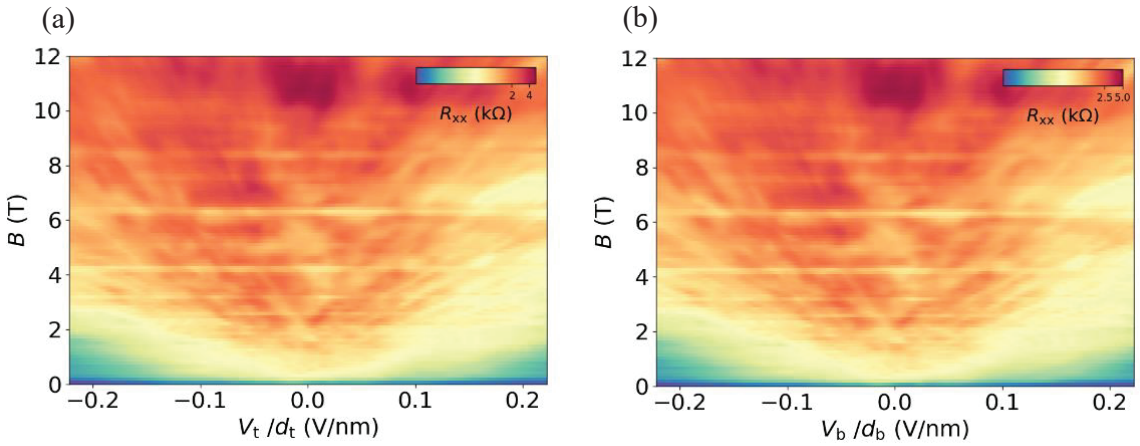

Figure 15. High field tansport of t7+7. R_{xx} Landau fans with (a) V_t sweep at V_b = 0 and (b) V_b sweep at V_t = 0.

obtained at low magnetic fields, where transport is mediated by the top and bottom surface states and the electron and hole free carriers in the bulk[57].

More interesting effects are observed in the ultra-quantum limit when a large perpendicular magnetic field B is applied. In conditions where we apply high B fields to Bernal graphite without a twisted interface, Landau fans show two distinct quantum oscillations where one set projects to zero gate voltage and the other projects to a gate voltage that is dependent on the bias applied to the opposite gate. This behavior arises because of the two lowest Landau levels in graphitic thin films. The N = 0 and N = 1 Landau bands are the only bands that cross the Fermi energy and as such electrons residing in these bands form standing waves throughout the bulk when a magnetic field is applied as described by the Manchester group[59].

In devices with a t1+Z configuration, drastically different behavior in transport is observed at high magnetic fields depending on whether we sweep the gate closest to the moiré interface or closest to the graphite surface. Sweeping V_{gr} with a fixed moiré potential results in two sets of quantum oscillations: 1) oscillations that project to V_{gr} = 0 that are independent of V_m and 2) states projecting to finite V_{gr} that are sensitive to V_m (Figure 13b, bottom left panel). We observe that the latter set of projection points track very closely to the zig-zag feature of

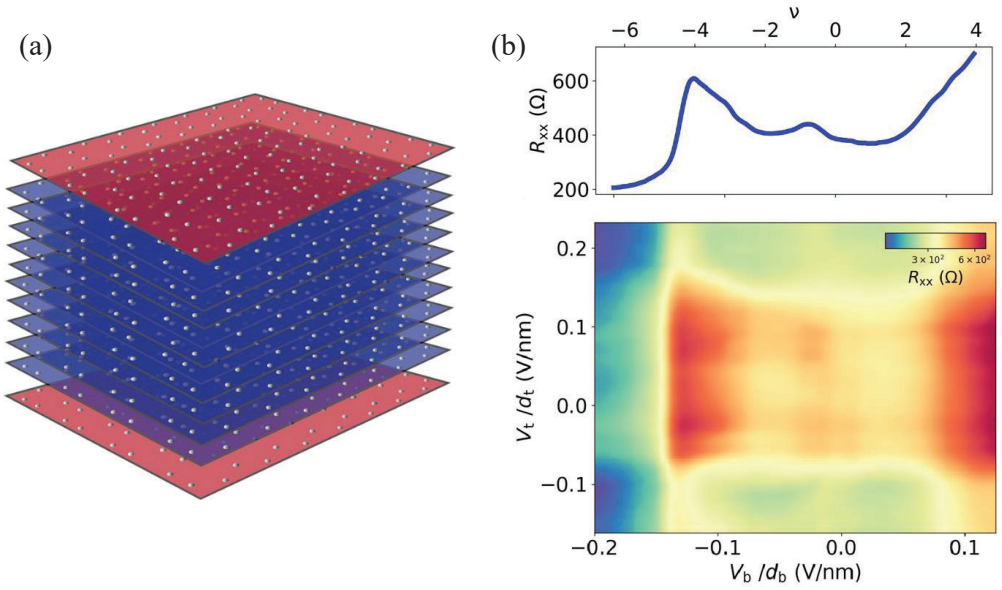

Figure 16. (a) Cartoon of graphite device with two moire interfaces. Red monolayer graphene is twisted at the same θ with respect to the blue graphitic film. (b) Zero-field transport R_{xx} map and $V_t/d_t = 0$ V/nm R_{xx} line-cut (top).

the R_{xy} map, suggesting that when the bulk states are doped, the oscillations are regulated by the moiré surface states. We can understand this as the standing wave hybridizing the moiré surface and bulk states.

In addition, we can also discuss the transport properties of two device configurations: 1) a device with 7 layers of Bernal graphite twisted with respect to another 7-layers of Bernal graphite (t7+7, Figure 12b) and 2) a device in a t1+11+1 configuration where a top and bottom monolayer graphene are rotated at an angle θ with respect to 11 layers of a Bernal stacked graphite (Figure 16a). Here, we have a moiré interface buried directly in the center (t7+7), and

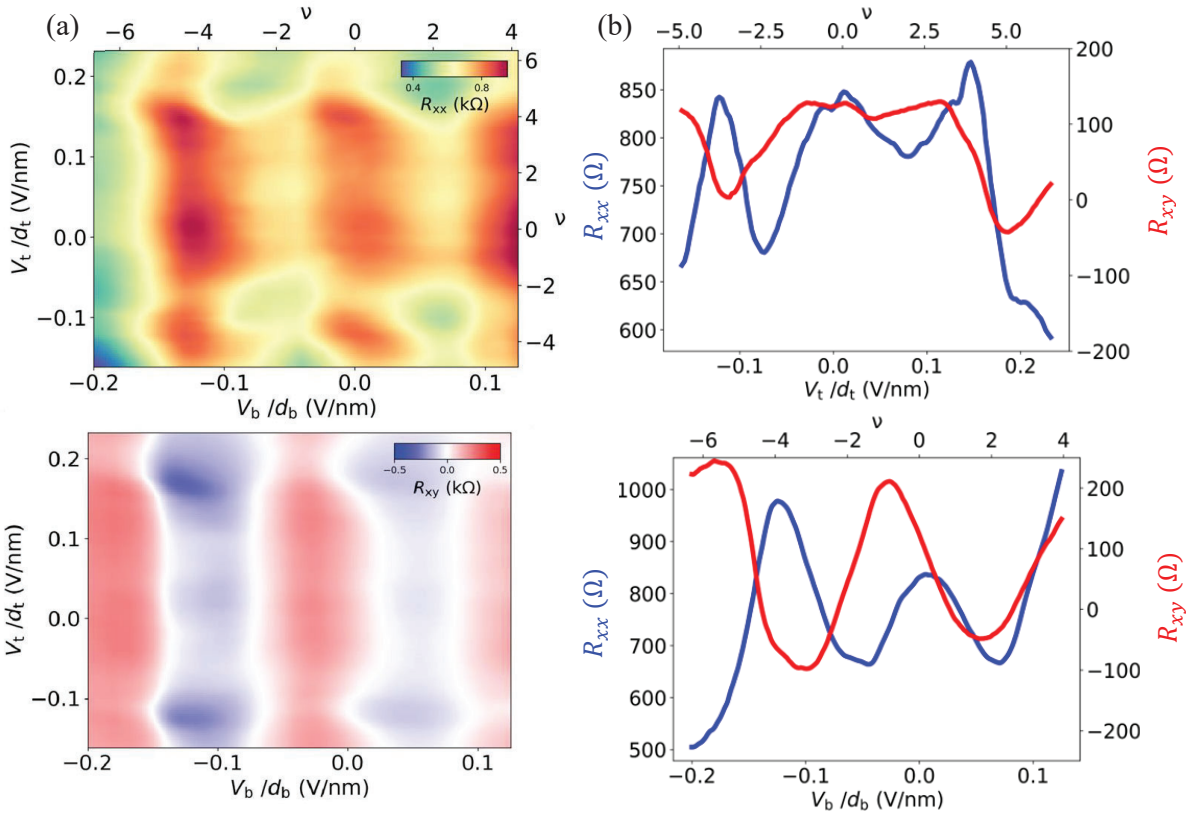

Figure 17. Low field magnetotransport of t1+11+1 device. (a) Longitudinal (top) and Hall (bottom) resistance as a function of top and bottom gate voltages. (b) Line cuts of R_{xx} and R_{xy} when $V_b = 0$ (top) and when $V_t = 0$ (bottom).

an additional moiré localized at an outer surface (t1+11+1). We find there is substantial change in the transport character of both systems compared to Bernal graphite, clearly implying the moiré potential can impart unconventional behavior in the properties of the bulk.

In Figure 14, we look at the longitudinal resistance as a function of top and bottom gate voltages. We see a change in R_{xx} that is comparable to the resistances observed when we sweep the graphite gate in the t1+10. However, the transport behavior at low field remains consistent when we hold one gate constant while sweeping the other, and we see only one resistance peak in R_{xx} (Figure 14b). We see this is consistent with the mirror symmetry of the device. It is important to also note that we do not observe band filling in the t7+7 system. Since the moiré is buried in the center of the device, it is inaccessible to gating. Nevertheless, Brown-Zak

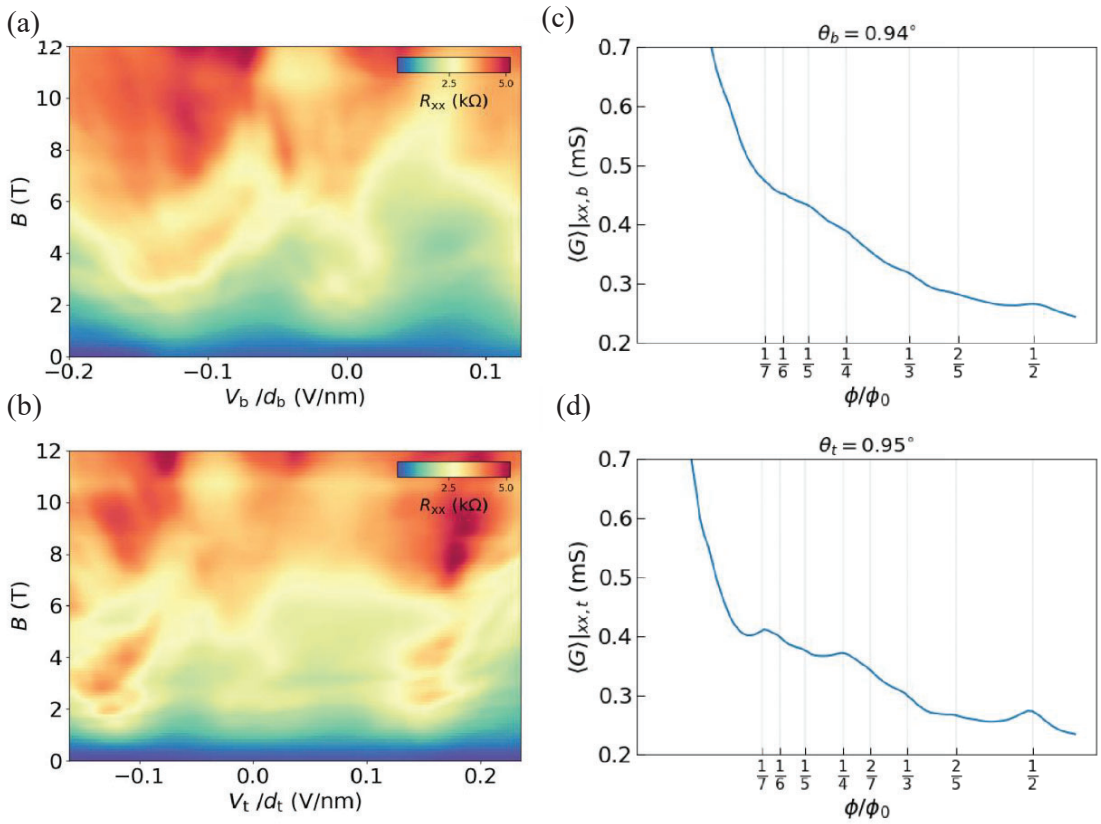

Figure 18. High field tansport of t1+11+1. R_{xx} Landau fans with (a) V_b sweep at V_t = 0 and (b) V_t sweep at V_b = 0. Magnetoconductance averaged across all gate voltages for (c) V_b and (d) V_t.

oscillations are clear in the Landau fan diagrams (Figure 15). The fans are taken by sweeping the top and bottom gates respectively and we can see they are nearly identical, further reflecting the high symmetry of the device.

Considering we observe moiré effects in devices with one moiré surface, we can also ask what happens when we have two moiré interfaces. A depiction of the t1+11+1 device is shown in Figure 16a. In the zero-field gate map, we see resistive peaks along V_b when we hold V_t/d_t = 0 V/nm, and vice versa (Figure 16b). We see similar behavior in comparison to the t1+10 device when we apply a 0.5T magnetic field (Figure 17). Maxima in R_{xx} occur at integer multiples of gate voltage that is required to fill the 4-fold degenerate moiré bands. As we expect, this phenomenon appears when we sweep both the top and bottom gates. Here, a zig-

zag trajectory is difficult to distinguish, and we see a stark contrast in R_{xy} behavior with prominent sign changes when we sweep the back gate for all values of V_t/d_t. On the other hand, there is little to no sign change in R_{xy} when we perform the same analysis across the top gate at fixed values of V_b/d_b. We cannot fully explain why there is asymmetry in the $R_{xy} = 0$ contour lines, but we suspect there may be differences in the electron mobility between the top and bottom moiré surfaces.

We have discussed the hybridization of the moiré with the bulk states in t1+Z systems. While sweeping the graphite gate, we saw quantum oscillations project to two points, including the trace of the zig-zag feature observed in the R_{xy} maps. In the t1+11+1 device, we were unable to identify quantum oscillation projections with certainty although we do observe QOs that project to integer filling factors corresponding to full filling and charge neutrality. Additionally, the presence of BZ oscillations (although rather weak) still confirm there is some degree of modulation by the twisted interfaces (Figure 18). However, it seems the addition of a moiré on one surface may interfere with the effects of the opposite moiré.

Overall, it is nevertheless surprising to see moiré effects in conditions in which we approach three-dimensions. We see the moiré can hybridize with the bulk states if it is confined to one surface in the ultra-quantum limit and can change the electrical transport of its bulk crystal regardless of whether we have a buried moiré, or a moiré on either or both surfaces. Ultimately, this experimental platform can be explored in other layered semimetals with low intrinsic bulk doping including WTe_2 and $ZrTe_5$.

Chapter 4: Electrical transport in double-twisted multilayered graphene structures

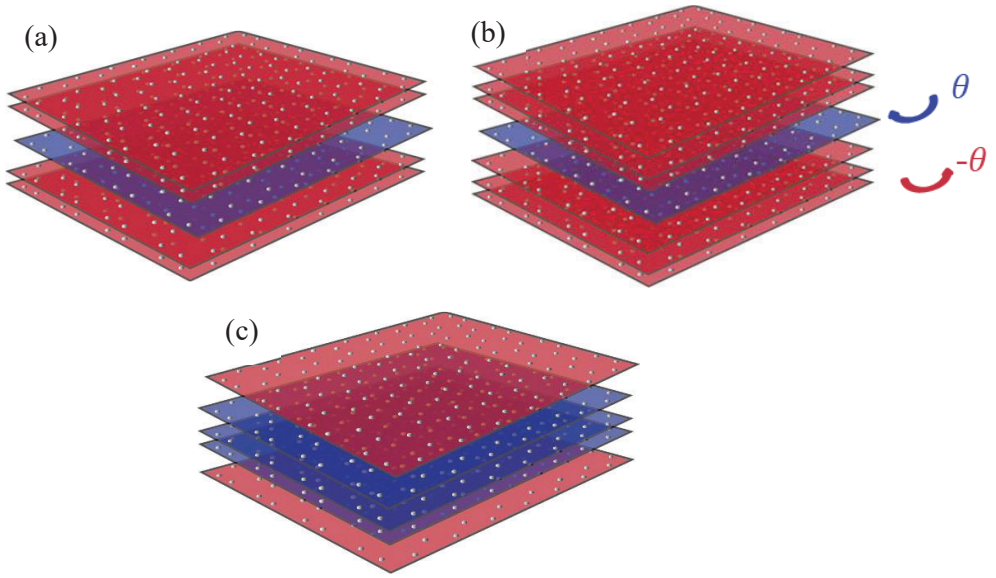

Figure 19. Cartoon schematic of (a) t2+1+2, (b) t3+1+3, and (c) t1+3+1. Red or blue colors denote layers that are twisted to an identical θ.

We have now seen how a twisted interface can alter the properties of a bulk graphite thin film. Now, we move our attention back to the thin limit and explore a material design with a distinct band structure. All the twisted structures we have described thus far can host flat bands near the Fermi level. In the bulk limit, we can have flat bands that coexist with the highly dispersive bands of bulk graphite. In thinner structures, one pair of flat bands are generally isolated from more dispersive bands by band gaps. Recently, a family of double-twisted structures has been described where we can have not one, but two pairs of isolated moiré flat bands at the Fermi level. Here, we will briefly describe transport properties of a t3+1+3 device and then move our attention to a t1+3+1 structure where double flat bands may be observed.

Band structures of double-twisted multilayer graphene

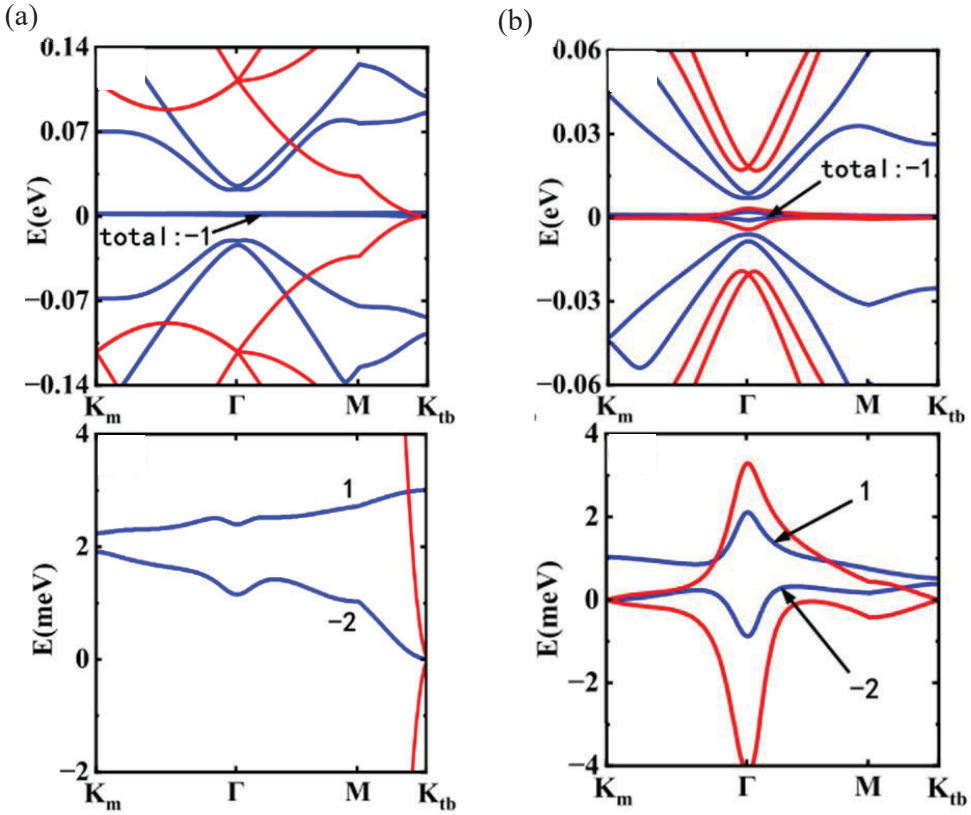

Figure 20. Band structures of (a) t2+1+2 for θ = 1.54° with enlarged view (bottom) and (b) t1+3+1 for θ = 1.05° with enlarged view (bottom). Adapted from[20].

Double-twisted graphene systems are arranged in a sandwich structure where a middle layer of one or more layers of graphene is enclosed between two monolayers or multilayers. The top and bottom sheets are rotated at the same angle θ, relative to the middle layer. We have seen this arrangement in alternating twisted trilayer graphene. In MATTG, the middle layer comprises a single graphene sheet. The Hamiltonian of MATTG can be decomposed into two subsystems considering the structure is mirror symmetric: 1) twisted bilayer graphene and 2) monolayer graphene. The MATTG was the second system to host the robust superconducting state and there is speculation that this property emerges due to the tBLG that appears in the Hamiltonian[20]. Other double-twisted structures can be decomposed in a similar way if they are also mirror symmetric.

The simplest cases of double-twist graphene systems with mirror symmetry are t1+3+1 and t2+1+2 as depicted in Figure 19. In general, any twisted system with tX+Y+X can be decomposed in a similar fashion. For a complete derivation of the mirror symmetric Hamiltonians, we refer the reader here[20].

Briefly, when Y = 1, a tX+Y+X system can be decoupled into a t1+X and a Bernal X-layer graphene. For example, the simplest case system, t2+1+2, can be decomposed into the following Hamiltonian,

$$H_{mirr,t2+1+2} = \begin{pmatrix} H_{tMBG} & 0 \\ 0 & H_{BLG} \end{pmatrix}$$

$$= \begin{pmatrix} H_1 & T_{1,2}^{\dagger} & 0 & 0 & 0 \\ T_{1,2} & H_2 & \sqrt{2}\tilde{T}_{2,3}^{\dagger} & 0 & 0 \\ 0 & \sqrt{2}\tilde{T}_{2,3} & H_3 & 0 & 0 \\ 0 & 0 & 0 & H_2 & T_{1,2} \\ 0 & 0 & 0 & T_{1,2}^{\dagger} & H_1 \end{pmatrix}$$

We can break down the structure into two subsystems that are twisted monolayer-bilayer graphene and Bernal bilayer graphene. The interlayer tunneling term $\tilde{T}$ is scaled by a factor of $\sqrt{2}$ so that the magic angle for the Y=1 case is $\theta = \sqrt{2} * 1.05° = 1.54°$. We can observe that the decomposition accurately reflects features observed in the bands structure calculations of t2+1+2 (Figure 20a). The flat bands arise from the H_{tMBG} and the parabolic bands at the K_{tb} point are a result of the Bernal bilayer graphene Hamiltonian.

We can also perform the same type of decomposition for a t3+1+3 structure (Figure 19b),

$$H_{mirr,t3+1+3} = \begin{pmatrix} H_{t1+3} & 0 \\ 0 & H_{TLG} \end{pmatrix}$$

$$= \begin{pmatrix} H_1 & T_{1,2}^{\dagger} & 0 & 0 & 0 & 0 & 0 \\ T_{1,2} & H_2 & T_{2,3}^{\dagger} & 0 & 0 & 0 & 0 \\ 0 & T_{2,3} & H_3 & \sqrt{2}\tilde{T}_{3,4}^{\dagger} & 0 & 0 & 0 \\ 0 & 0 & \sqrt{2}\tilde{T}_{3,4} & H_4 & 0 & 0 & 0 \\ 0 & 0 & 0 & 0 & H_3 & T_{2,3} & 0 \\ 0 & 0 & 0 & 0 & T_{2,3}^{\dagger} & H_2 & T_{1,2} \\ 0 & 0 & 0 & 0 & 0 & T_{1,2}^{\dagger} & H_1 \end{pmatrix}.$$

Here, the t3+1+3 Hamiltonian is decoupled into twisted monolayer-trilayer graphene (t1+3) and trilayer graphene (TLG). The decomposition allows us to gain intuition about what the

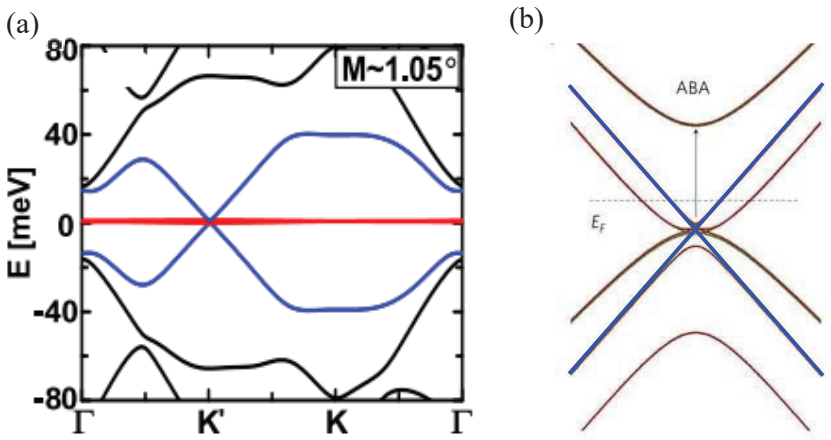

Figure 21. Band structures of (a) t1+3 for θ = 1.05° and (b) ABA-trilayer. Reprinted with permission[61,62].

band structure of t3+1+3 may look like. Figure 21 depicts the two band structures of the mirror decomposition. We can make an educated guess that the band structure of the t3+1+3 will have Dirac bands touching at both K points as both t1+3 and ABA-trilayer contain linear bands (denoted in blue). However, it is likely only one pair of the bands will hybridize, since there is only one moiré interface in H_{t1+3}. The band structures of t2+1+2 and t3+1+3 therefore only have one pair of flat bands.

Performing the same analysis but with Y ≠ 0 results in a decoupling that comprises two twisted subsystems. The t1+3+1 is the simplest structure of this family of double-twisted multilayer graphene. The decomposed Hamiltonian is of the form,

$$H_{mirr,t1+3+1} = \begin{pmatrix} H_{tMBG} & 0 \\ 0 & H_{tBLG} \end{pmatrix}$$

$$= \begin{pmatrix} H_1 & \tilde{T}_{1,2}^{\dagger} & 0 & 0 & 0 \\ \tilde{T}_{1,2} & H_2 & \sqrt{2}T_{2,3}^{\dagger} & 0 & 0 \\ 0 & \sqrt{2}T_{2,3} & H_3 & 0 & 0 \\ 0 & 0 & 0 & H_2 & \tilde{T}_{1,2} \\ 0 & 0 & 0 & \tilde{T}_{1,2}^{\dagger} & H_1 \end{pmatrix}$$

Here the system is an amalgamation of twisted monolayer bilayer and twisted bilayer graphene. The magic angle for t1+3+1 remains the same as that of tMBG and tBLG ($\theta = 1.05°$) since the $\sqrt{2}$ term does not reside at $\tilde{T}$, and therefore does not have a significant influence on the band structure near the Fermi level. More importantly, the decomposition clearly interprets the double-flat bands present in band structure calculations (Figure 20b). One band is formed from the tMBG and the other results from the twisted bilayer graphene. In general, double-flat bands are thought to materialize under the conditions where the graphitic material must be a sandwiched double-twisted structure, and the middle layer must contribute multiple bands at low energy (i.e. the middle layer Y ≥ 3 layers)[18,19]. Systems such as the t1+3+1 with four-fold degenerate moiré flat bands have never been studied in experiment before. The question we aim to investigate is whether we can observe band filling of double-flat bands in electrical transport measurements and, more importantly, whether a system with two pairs of flat bands can host unique physical phenomena.

Band filling in double-twisted trilayer-monolayer-trilayer graphene

Figure 22 shows the resistance maps of device t3+1+3 with a twist angle $\theta = 1.58°$ as a function of displacement field and filling factor. The band structure of the t3+1+3 structure can be compared to the t1+3 and ABA-trilayer case. In Figure 22a and b, we can see features at full filling of the moiré bands and near the charge neutrality point. The insulating feature at $\nu = -4$ has a prominent R_{xx} peak while the feature at $\nu = 4$ is less than 1 kΩ. At charge neutrality a gap starts to emerge at large displacement field $|D|$, although it remains relatively weak. Further moiré modulation is observed as quantum oscillations in the Landau fans that project to $\nu = \pm 4$ and the presence of BZ oscillations (Figure 22c and d). However, we do not observe any features that may indicate the presence of non-trivial states.

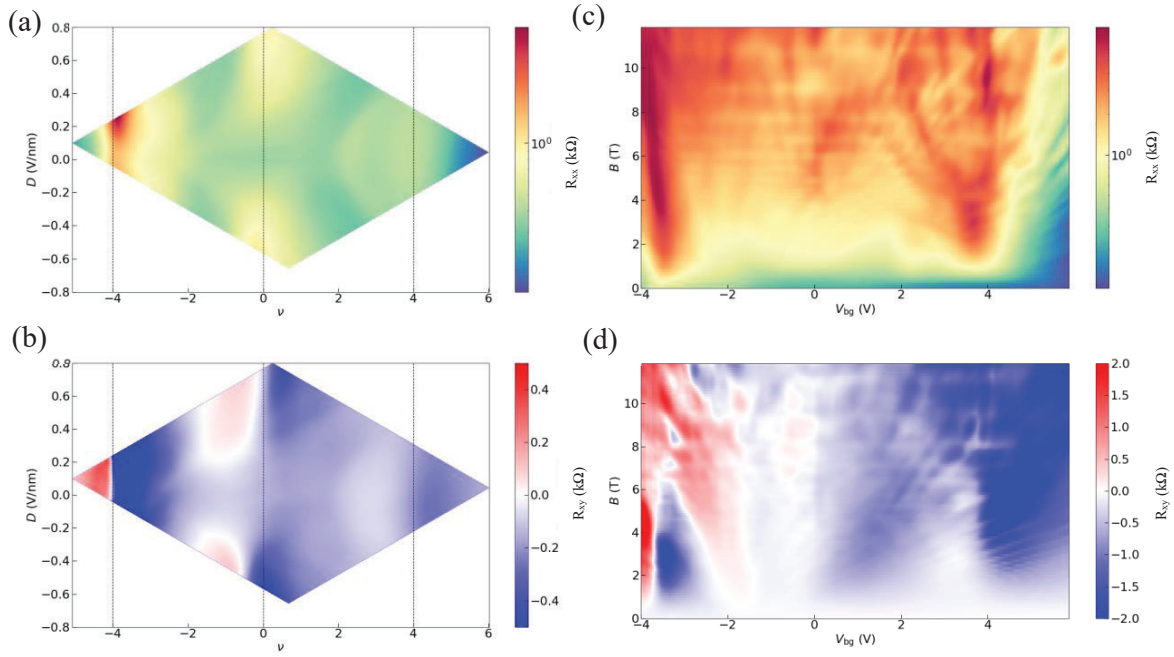

Figure 22. Low field transport and Landau fan diagrams of t3+1+3. (a) R_{xx} and (b) R_{xy} maps as a function of filling factor ν and displacement field D. Back gate (c) R_{xx} and (d) R_{xy} Landau fans depicting BZ oscillations.

Possible double-band filling in t1+3+1

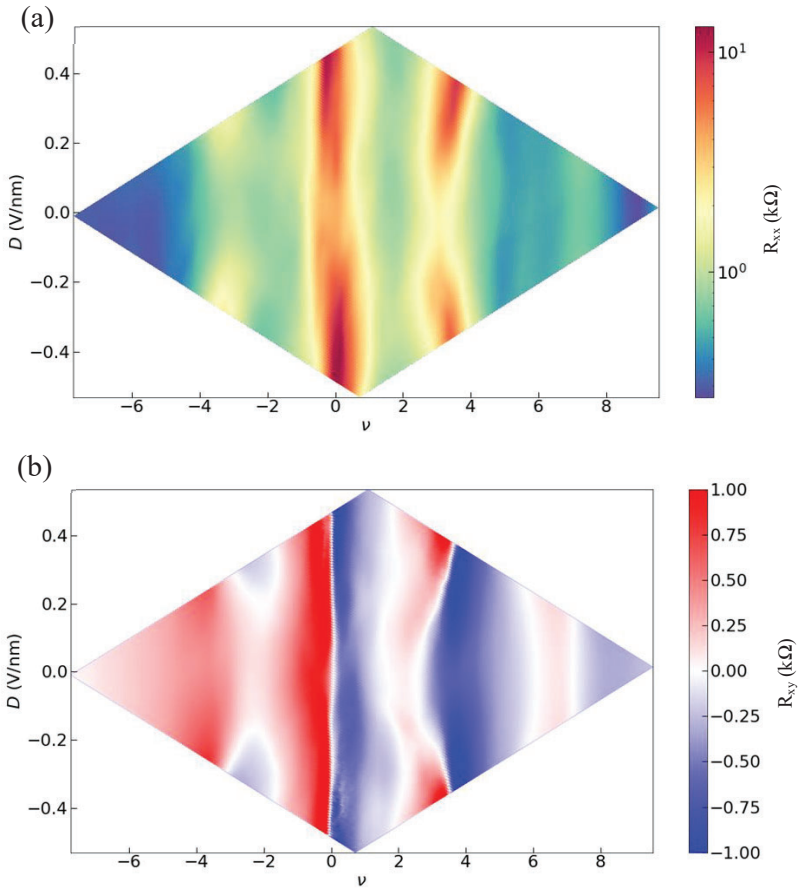

Figure 23. Low-field magnetotransport of t1+3+1. (a) Longitudinal and (b) Hall resistance maps acquired at B = 0.5T.

Figure 23a shows the longitudinal resistance, R_{xx}, at finite magnetic field as a function of the filling factor, ν, and displacement field for a t1+3+1 device with a twist angle θ = 1.08°. We see primary resistance features that we can assign to full filling at $\nu = \pm 4$ and the CNP at ν = 0. An increase in the resistance maxima is seen as we increase the $|D|$ field for these values of ν. Ding et. al. have also predicted that an electric field may lift the degeneracy and isolate the flat bands[20]. Thus, we may expect to see additional gaps in the resistance maps that could potentially correspond to a filling factor of ν = 8. In the Hall resistance maps (Figure 23b) we see changes in the sign of charge carriers most clearly at charge neutrality and $\nu = \pm 4$. The insulating state at $\nu = +4$ also seems to arise from a van Hove singularity which begs the

question of whether we have a trivial or correlated state. There is also a sign change past $\nu = 4$ which may indicate the presence of additional states. However, it is necessary to further inquire whether our filling factor assignments are accurate.

Since it is not immediately clear whether we have observed filling of a second moiré band corresponding to $\nu = 8$, we can gain a better understanding by examining Landau fans at fixed values of D field (Figure 24). The top Landau fan in Figure 24 is taken at $D = 0$ V/nm as a function of back gate voltage (V_{bg}) and perpendicular magnetic field up to 12T. Sequences of quantum oscillations appear when there is a dip in resistance and are denoted with dotted lines. These reveal points that project to integer filling factors of the moiré. There appear to be projection points near 0V and ± 3V, and unexpectedly, we see QOs projecting to a location near $V_{bg} \approx 6$V. We can observe the QOs clearly in the corresponding $D = 0$ V/nm R_{xy} map and assign the QOs at $V_{bg} \approx 6$V to $\nu = 8$. Due to device constraints, we are not able to observe QOs past $V_{bg} = -3$V which makes it difficult to confirm that we have observed filling of two bands. Regardless, the projections seem consistent with the filling of two moiré bands as we look at more Landau fans at finite displacement field.

At low displacement field, $D = 0$ V/nm, we have seen quantum oscillations that appear to project to trivial insulating states corresponding to full fillings of the moiré minibands. As we move to higher displacement fields ($|D| = 4$ V/nm), resistive states start to emerge more clearly at $\nu = 2$. These resistive states are most prominently seen in the R_{xx} maps. There is a clear resistive state at high magnetic fields ($B \approx 12$T). We also observed oscillations projecting to $\nu = \pm 1$ when $D = 0.25$ V/nm, although no prominent resistive state was observed for these filling factors (not pictured). Although the resistive states projecting to $\nu = 2$ follow the Hofstadter spectrum of allowed states, there remains a high chance that the states we are seeing

are non-trivial correlated states. However, further studies are warranted considering the added complication of having two pairs of flat bands.

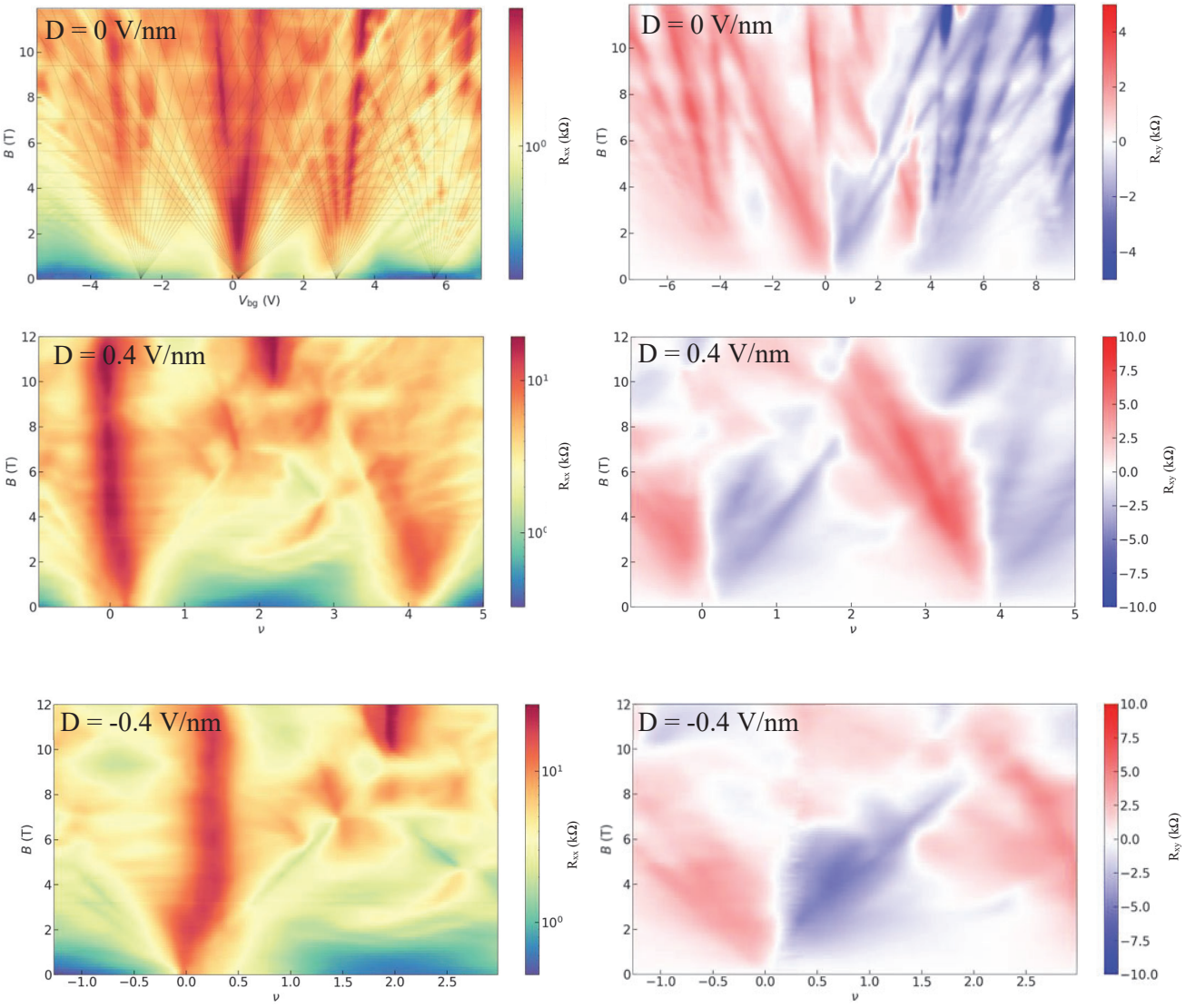

Figure 24. R_{xx} (right) and R_{xy} (left) Landau fan diagrams of t1+3+1 device acquired by sweeping V_{bg} and fitting to corresponding filling factors ν for finite displacement field D.

Chapter 5: Conclusions and Outlook

In this work we have demonstrated two promising platforms in which moiré potentials can control the properties of multilayered graphene systems.

Our results studying structures in the bulk graphite limit have shown that moiré potentials localized at the surface of graphitic films can dramatically alter the properties of the entire crystal. This includes moiré potentials located at the top and bottom surfaces of the graphite stack and when a moiré interface is buried in the middle. Band structure calculations first demonstrated that a flat band could coexist with dispersive graphite bands. We have now uncovered a mechanism by which a moiré potential can change transport in graphite. We saw that a standing wave can hybridize the moiré's with bulk states as demonstrated by the presence of Brown-Zak oscillations in Landau fans. However, further studies are needed to determine if we can observe quantum oscillations projecting to moiré and bulk states in the t1+11+1 structure.

Furthermore, the double-twisted multilayered graphene, t1+3+1, was also known to exhibit a distinct band structure. In this system, the hybridization of two pairs of bands is possible. The mirror decomposition presented in Chapter 4 also hints at the possibility of finding superconductivity in a double twisted t1+3+1 system, since it shares equivalent Hamiltonians with tBLG. The data presented here reflects the complexity of the band structure. We observe what appears to be band filling of two pairs of moiré flat bands although more studies are required to fully understand the phenomena. We also observe prominent states at high magnetic fields. We see resistive states start to emerge and project to filling factors in both the valence and conduction band. The most notable feature is the insulator at $\nu = 2$ that appears

at high field. Further experiments at millikelvin temperatures will be performed to elucidate the nature of the high field resistive states.

Among the family of twisted multilayered graphene structures that have been studied to date, only a few systems have been shown to host a robust superconducting state: twisted bilayer graphene and, more broadly, the twisted alternating graphene family. The exact conditions required to realize superconductivity is still under question. The systems presented in this paper, mixed-dimensional systems and double-twisted multilayered graphene, offer promising platforms to further understand many-body phenomena and ultimately shed light on the nature of the superconducting state.

References

1. Geim, A. K. & Novoselov, K. S. The rise of graphene. *Nat Mater* **6**, 183–191 (2007).

2. Novoselov, K. S. *et al.* Electric Field Effect in Atomically Thin Carbon Films. *Science (1979)* **306**, 666–669 (2004).

3. Takai, Kazuyuki., Tsujimura, Seiya., Kang, Feiyu. & Inagaki, Michio. *Graphene : preparations, properties, applications and prospects*. (Elsevier, 2020).

4. Geim, A. K. & Grigorieva, I. v. Van der Waals heterostructures. *Nature* **499**, 419–425 (2013).

5. Liu, Y. *et al.* Van der Waals heterostructures and devices. *Nat Rev Mater* **1**, 16042 (2016).

6. Ganatra, R. & Zhang, Q. Few-Layer MoS2: A Promising Layered Semiconductor. *ACS Nano* **8**, 4074–4099 (2014).

7. Manzeli, S., Ovchinnikov, D., Pasquier, D., Yazyev, O. v & Kis, A. 2D transition metal dichalcogenides. *Nat Rev Mater* **2**, 17033 (2017).

8. Yankowitz, M., Ma, Q., Jarillo-Herrero, P. & LeRoy, B. J. van der Waals heterostructures combining graphene and hexagonal boron nitride. *Nature Reviews Physics* **1**, 112–125 (2019).

9. Zhong, D. *et al.* Layer-resolved magnetic proximity effect in van der Waals heterostructures. *Nat Nanotechnol* **15**, 187–191 (2020).

10. Tseng, C.-C. *et al.* Gate-Tunable Proximity Effects in Graphene on Layered Magnetic Insulators. *Nano Lett* **22**, 8495–8501 (2022).

11. Cao, Y. *et al.* Correlated insulator behaviour at half-filling in magic-angle graphene superlattices. *Nature* **556**, 80–84 (2018).

12. Cao, Y. *et al.* Unconventional superconductivity in magic-angle graphene superlattices. *Nature* **556**, 43–50 (2018).

13. Yankowitz, M. *et al.* Tuning superconductivity in twisted bilayer graphene. *Science (1979)* **363**, 1059–1064 (2019).

14. Chen, S. *et al.* Electrically tunable correlated and topological states in twisted monolayer–bilayer graphene. *Nat Phys* **17**, 374–380 (2021).

15. Xie, Y. *et al.* Fractional Chern insulators in magic-angle twisted bilayer graphene. *Nature* **600**, 439–443 (2021).

16. Castro Neto, A. H., Guinea, F., Peres, N. M. R., Novoselov, K. S. & Geim, A. K. The electronic properties of graphene. *Rev Mod Phys* **81**, 109–162 (2009).

17. McCann, E. & Koshino, M. The electronic properties of bilayer graphene. *Reports on Progress in Physics* **76**, 056503 (2013).

18. Xie, B., Peng, R., Zhang, S. & Liu, J. Alternating twisted multilayer graphene: generic partition rules, double flat bands, and orbital magnetoelectric effect. *NPJ Comput Mater* **8**, 110 (2022).

19. Ma, Z. *et al.* Doubled Moiré flat bands in double-twisted few-layer graphite. *Sci China Phys Mech Astron* **66**, 227211 (2023).

20. Ding, S.-P., Liang, M., Ma, Z., Lü, J.-T. & Gao, J.-H. Mirror symmetry decomposition in double-twisted multilayer graphene systems. *ArXiv* (2022).

21. Novoselov, K. S. *et al.* Two-dimensional gas of massless Dirac fermions in graphene. *Nature* **438**, 197–200 (2005).

22. Stormer, H. L. Two-dimensional electron correlation in high magnetic fields. *Physica B Condens Matter* **177**, 401–408 (1992).

23. McCann, E., Abergel, D. S. L. & Fal'ko, V. I. The low energy electronic band structure of bilayer graphene. *The European physical journal. ST, Special topics* **148**, 91–103 (2007).

24. McCann, E. & Fal'ko, V. I. Landau-level degeneracy and quantum Hall effect in a graphite bilayer. *Phys Rev Lett* **96**, 86805 (2006).

25. Zhang, Y. *et al.* Landau-Level Splitting in Graphene in High Magnetic Fields. *Phys. Rev. Lett.* **96**, 136806 (2006).

26. Cao, Y. *et al.* Superlattice-Induced Insulating States and Valley-Protected Orbits in Twisted Bilayer Graphene. *Phys Rev Lett* **117**, 116804 (2016).

27. Zhang, Y.-H., Po, H. C. & Senthil, T. Landau level degeneracy in twisted bilayer graphene: Role of symmetry breaking. *Phys Rev B* **100**, (2019).

28. Novoselov, K. S., Mishchenko, A., Carvalho, A. & Neto, A. H. C. 2D materials and van der Waals heterostructures. *Science (1979)* **353**, aac9439 (2016).

29. Wang, Z., Tang, C., Sachs, R., Barlas, Y. & Shi, J. Proximity-Induced Ferromagnetism in Graphene Revealed by the Anomalous Hall Effect. *Phys Rev Lett* **114**, 016603 (2015).

30. Leutenantsmeyer, J. C., Kaverzin, A. A., Wojtaszek, M. & van Wees, B. J. Proximity induced room temperature ferromagnetism in graphene probed with spin currents. *2d Mater* **4**, 014001 (2017).

31. Tseng, C.-C. *et al.* Gate-Tunable Proximity Effects in Graphene on Layered Magnetic Insulators. *Nano Lett* **22**, 8495–8501 (2022).

32. Fang, H. *et al.* Strong interlayer coupling in van der Waals heterostructures built from single-layer chalcogenides. *Proceedings of the National Academy of Sciences* **111**, 6198–6202 (2014).

33. Rivera, P. *et al.* Observation of long-lived interlayer excitons in monolayer MoSe2–WSe2 heterostructures. *Nat Commun* **6**, 6242 (2015).

34. Kim, J. *et al.* Observation of ultralong valley lifetime in WSe2/MoS2 heterostructures. *Sci Adv* **3**, e1700518 (2023).

35. Bistritzer, R. & MacDonald, A. H. Moiré bands in twisted double-layer graphene. *Proceedings of the National Academy of Sciences* **108**, 12233–12237 (2011).

36. Zibrov, A. A. *et al.* Tunable interacting composite fermion phases in a half-filled bilayer-graphene Landau level. *Nature* **549**, 360–364 (2017).

37. Watanabe, K., Taniguchi, T. & Kanda, H. Direct-bandgap properties and evidence for ultraviolet lasing of hexagonal boron nitride single crystal. *Nat Mater* **3**, 404–409 (2004).

38. Dean, C. R. *et al.* Boron nitride substrates for high-quality graphene electronics. *Nat Nanotechnol* **5**, 722–726 (2010).

39. Nuckolls, K. P. *et al.* Strongly correlated Chern insulators in magic-angle twisted bilayer graphene. *Nature (London)* **588**, 610–615 (2020).

40. Ma, L. *et al.* Strongly correlated excitonic insulator in atomic double layers. *Nature* **598**, 585–589 (2021).

41. Sharpe, A. L. *et al.* Emergent ferromagnetism near three-quarters filling in twisted bilayer graphene. *Science (1979)* **365**, 605–608 (2019).

42. Wang, L. *et al.* Correlated electronic phases in twisted bilayer transition metal dichalcogenides. *Nat Mater* **19**, 861–866 (2020).

43. Zhou, H., Xie, T., Taniguchi, T., Watanabe, K. & Young, A. F. Superconductivity in rhombohedral trilayer graphene. *Nature* **598**, 434–438 (2021).

44. Park, J. M., Cao, Y., Watanabe, K., Taniguchi, T. & Jarillo-Herrero, P. Tunable strongly coupled superconductivity in magic-angle twisted trilayer graphene. *Nature* **590**, 249–255 (2021).

45. Cao, Y., Park, J. M., Watanabe, K., Taniguchi, T. & Jarillo-Herrero, P. Pauli-limit violation and re-entrant superconductivity in moiré graphene. *Nature* **595**, 526–531 (2021).

46. Park, J. M. *et al.* Robust superconductivity in magic-angle multilayer graphene family. *Nat Mater* **21**, 877–883 (2022).

47. Zhang, Y. *et al.* Promotion of superconductivity in magic-angle graphene multilayers. *Science (1979)* **377**, 1538–1543 (2022).

48. Rickhaus, P. *et al.* Correlated electron-hole state in twisted double-bilayer graphene. *Science (1979)* **373**, 1257–1260 (2021).

49. He, M. *et al.* Symmetry breaking in twisted double bilayer graphene. *Nat Phys* **17**, 26–30 (2021).

50. Wang, Y. *et al.* Bulk and edge properties of twisted double bilayer graphene. *Nat Phys* **18**, 48–53 (2022).

51. He, M. *et al.* Competing correlated states and abundant orbital magnetism in twisted monolayer-bilayer graphene. *Nat Commun* **12**, 4727 (2021).

52. Wang, L. *et al.* One-Dimensional Electrical Contact to a Two-Dimensional Material. *Science (1979)* **342**, 614–617 (2013).

53. Hofstadter, D. R. Energy levels and wave functions of Bloch electrons in rational and irrational magnetic fields. *Physical review. B, Solid state* **14**, 2239–2249 (1976).

54. Hunt, B. *et al.* Massive Dirac Fermions and Hofstadter Butterfly in a van der Waals Heterostructure. *Science (1979)* **340**, 1427–1430 (2013).

55. Krishna Kumar, R. *et al.* High-temperature quantum oscillations caused by recurring Bloch states in graphene superlattices. *Science (1979)* **357**, 181–184 (2017).

56. Cea, T., Walet, N. R. & Guinea, F. Twists and the Electronic Structure of Graphitic Materials. *Nano Lett* **19**, 8683–8689 (2019).

57. Waters, D. *et al.* Mixed-dimensional moiré systems of graphitic thin films with a twisted interface. *ArXiv* (2022).

58. Koshino, M. Interlayer screening effect in graphene multilayers with ABA and ABC stacking. *Phys Rev B* **81**, 125304 (2010).

59. Yin, J. *et al.* Dimensional reduction, quantum Hall effect and layer parity in graphite films. *Nat Phys* **15**, 437–442 (2019).

60. Peng, Z., Chen, X., Fan, Y., Srolovitz, D. J. & Lei, D. Strain engineering of 2D semiconductors and graphene: from strain fields to band-structure tuning and photonic applications. *Light Sci Appl* **9**, 190 (2020).

61. Ma, Z. *et al.* Moiré flat bands of twisted few-layer graphite. *Front Phys (Beijing)* **18**, 13307 (2022).

62. Lui, C. H., Li, Z., Mak, K. F., Cappelluti, E. & Heinz, T. F. Observation of an electrically tunable band gap in trilayer graphene. *Nat Phys* **7**, 944–947 (2011).